Electronic Supplementary Material (ESI) for Energy & Environmental Science.
This journal is © The Royal Society of Chemistry 2020

*Supplementary information*

# Multiorbital Bond Formation for Stable Oxygen-Redox Reaction in Battery Electrodes

Takaaki Sudayama[1], Kazuki Uehara[2], Takahiro Mukai[3], Daisuke Asakura[1], Xiang-Mei Shi,[2] Akihisa Tsuchimoto,[2] Benoit Mortemard de Boisse[2,4], Tatau Shimada[2], Eriko Watanabe[2], Yoshihisa Harada[5], Masanobu Nakayama[3,4,6], Masashi Okubo[2,4], Atsuo Yamada[2,4],*

[1]Research Institute for Energy Conservation, National Institute of Advanced Industrial Science and Technology, Tsukuba, Ibaraki 305-8568, Japan

[2]Department of Chemical System Engineering, School of Engineering, The University of Tokyo, Bunkyo-ku, Tokyo 113-8656, Japan

[3]Frontier Research Institute for Materials Science (FRIMS), Nagoya Institute of Technology, Showa-ku, Nagoya, Aichi 466-8555, Japan

[4]Elements Strategy Initiative for Catalysts & Batteries (ESICB), Kyoto University, Nishikyo-ku, Kyoto 615-8245, Japan

[5]Institute for Solid State Physics, The University of Tokyo, Kashiwa, Chiba 277-8581, Japan

[6]Mi[2]i GREEN, National Institute of Materials Science (NIMS), Tsukuba, Ibaraki, 305-0047, Japan

*yamada@chemsys.t.u-tokyo.ac.jp

**Genetic algorithm details**

The structural configuration of $Li_{1.2}Ni_{0.13}Co_{0.13}Mn_{0.54}O_2$ was determined by the genetic algorithm (GA) that optimizes the Li/Ni/Co/Mn arrangement. During this optimization, the molar ratio of Li/Ni/Co/Mn was set as 29/3/3/13, *i.e.*, $Li_{29/24}Ni_{3/24}Co_{3/24}Mn_{13/24}O_2$ to best reproduce the experimental composition. A supercell (96 atoms) of a layered rock-salt type $LiCoO_2$ hexagonal structure (*Rm*) was used as an initial model. The octahedral 3*a* sites are fully occupied by Li ions (Li-only layer), while the octahedral 3*b* sites are occupied by transition metal ions, (TM: Ni, Co, Mn) and Li. The arrangement of the 3*b*-site cations was optimized by GA approach, as the total energy is the lowest. In the GA, cation arrangement is regarded as a quaternary string consisting of four labels, 0 (Li), 1 (Co), 2 (Mn), and 3 (Ni), and each cationic site is assigned to a specific string index. Therefore, the string size is 48, and the conceivable combination of quaternary strings is approximately $2.3 \times 10^{10}$ without considering the symmetrical duplicates.

We first prepared 20 configurations (quaternary strings), where Li, Co, Ni, and Mn ions were arranged randomly at the octahedral 3*b* sites (first generation), and computed the total electron energies based on DFT PBEsol-GGA. Twelve low energy configurations among twenty candidates (60 %) were selected as survivors and their structural features were succeeded to the next generation by the following four options. (1) Three best structures succeeded as they were, (2) eight new structures were created by two-point crossover technique, (3) eight structures were created by half-uniform crossover technique, and (4) four structures were created by mutation techniques. The algorithm for travelling salesman problem (TSP) was adopted to maintain the composition (molar ratio of Li/Co/Ni/Mn ions) during the above four gene manipulations. The generated structures were selected not to be consistent with the previously calculated configuration (random cation arrangement is chosen if the above genetic operation cannot produce new structure). By repeating this procedure, the lowest energy configuration was determined heuristically. Note that we obtained the total energies during GA procedure by reducing the energy cutoff and number of k points in the reciprocal cell to 360 eV and unity (Γ point

sampling), respectively, to speed up the calculation as the total energies of around 1600 configurations had to be evaluated. After GA cycles, the obtained lowest-energy configurations were recalculated with sufficient energy cutoff (500 eV) and *k*-point mesh (2×2×2 *k*-point meshes) using HSE06 hybrid functional. Figure S6a represents the total energy distribution of GA-derived structures as the function of a generation (up to 72 generations). The best structure (lowest energy structure) is displayed in Figure S6b. Furthermore, we used the TM configuration shown in Figure S6c for the electrochemically delithiated phase calculation, unless specially mentioned.

The Li and vacancy configurations for delithiated $Li_{29/24(1-x)}Ni_{3/24}Co_{3/24}Mn_{13/24}O_2$ were determined by GA approach using DFT PBEsol-GGA functional. The structure relaxation for GA-driven delithiated structures was performed using HSE06 hybrid functional. We confirmed that the TM ions occupied the octahedral cation sites without significant modification of lattice, even for the fully delithiated composition ($x$=1.0, Figure S6c).

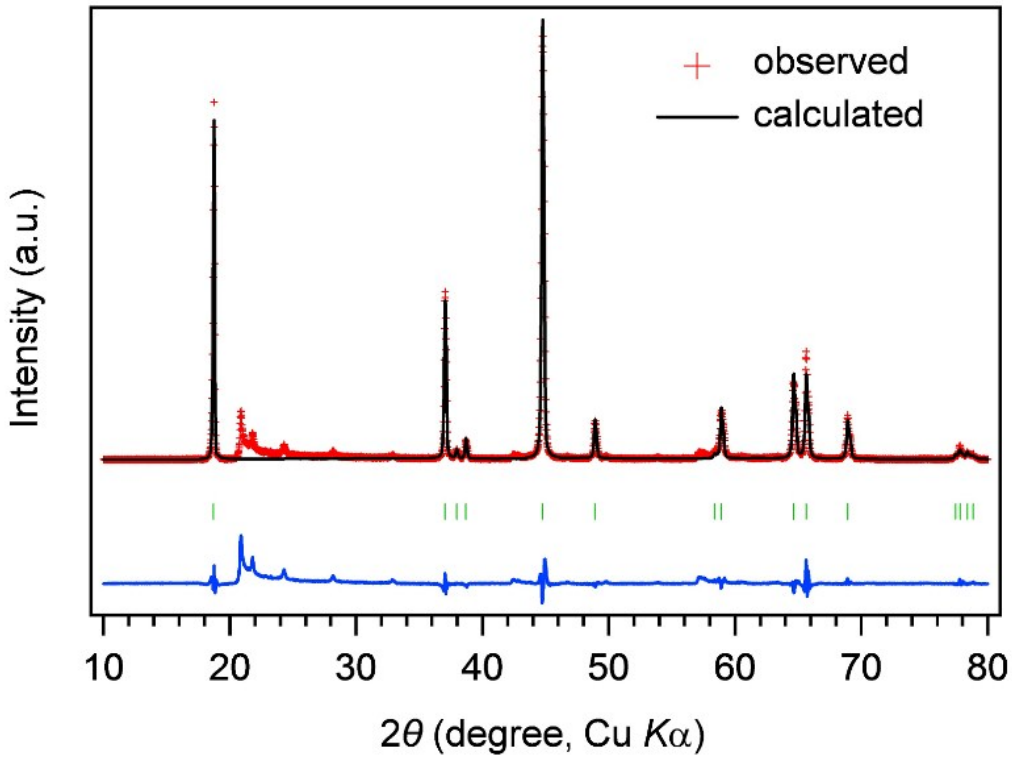


**Figure S1.** X-ray diffraction pattern for $Li_2MnO_3$. The Rietveld refinement result is also plotted. Superstructure peaks ($20° < 2\theta < 30°$) broadened by stacking faults were ignored in the Rietveld refinement, as the stacking faults are not the focus of this work.

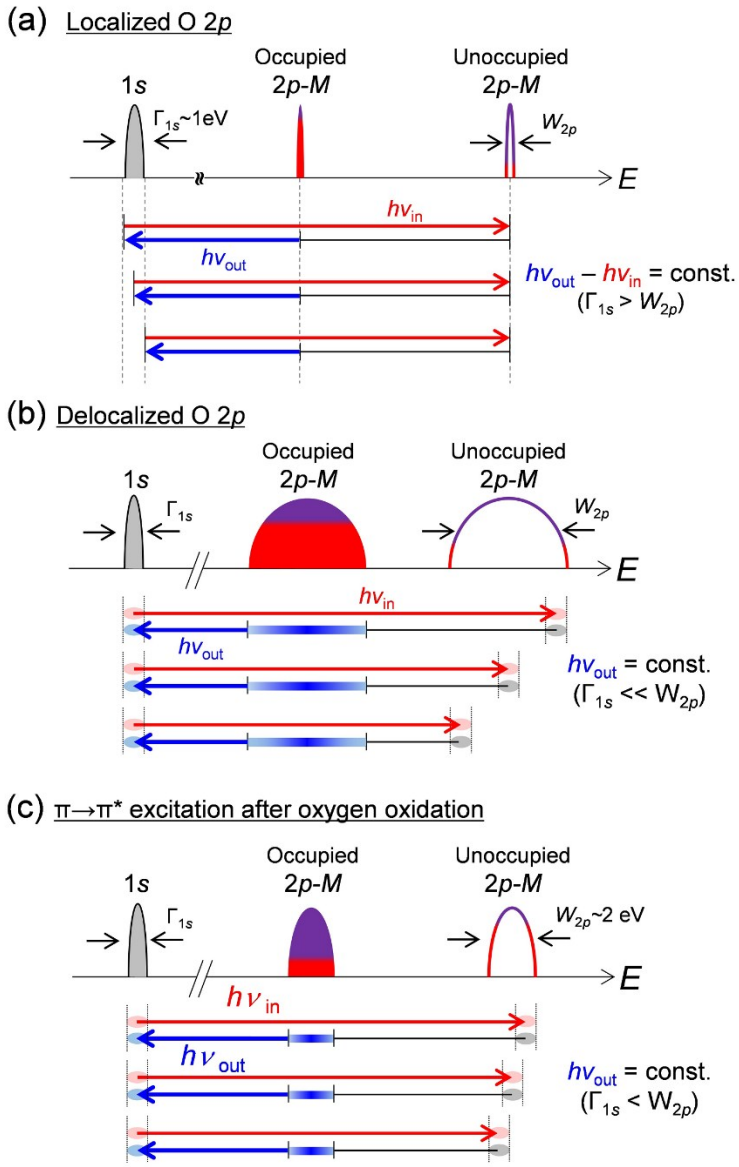


**Figure S2.** Energy diagram of delocalized and localized oxygen 2*p* orbitals for resonant inelastic X-ray scattering (RIXS) spectra. (a) Localized O 2*p* bands give a RIXS peak with constant energy loss for the case where the inverse of the lifetime of core hole ($\Gamma_{1s}$) is longer than the O 2*p* band width ($W_{2p}$). (b) Delocalized O 2*p* bands give a RIXS peak with variable energy loss for $\Gamma_{1s} << W_{2p}$. (c) π→π* excitation after oxygen oxidation with variable energy loss for $W_{2p} \sim 2$ eV ($> \Gamma_{1s}$).

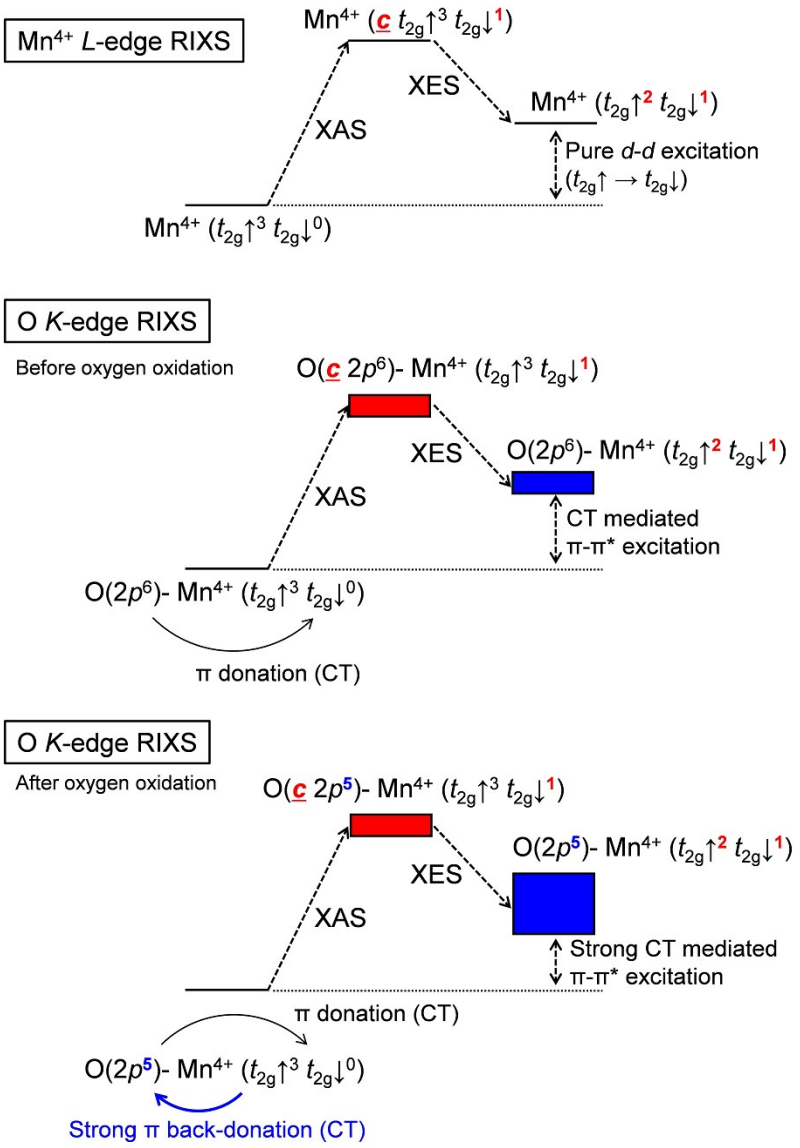


**Figure S3.** Absorption/emission processes in $Mn^{4+}$ *L*-edge RIXS, O *K*-edge RIXS for conventional oxides, and O *K*-edge RIXS for oxides after oxygen oxidation. *c* denotes core hole. Mn *L*-edge exhibits pure *d*-*d* excitation without charge transfer (CT). However, for O *K*-edge, as 2*p* orbitals of $O^{2-}$ are fully occupied at the ground state, charge transfer interaction between O and Mn (π donation) is needed for RIXS processes. After oxygen oxidation, O 2*p* orbital becomes partially unoccupied, which gives rise to strong π back-donation from Mn. This strong CT after oxygen oxidation allows for diverse RIXS processes.

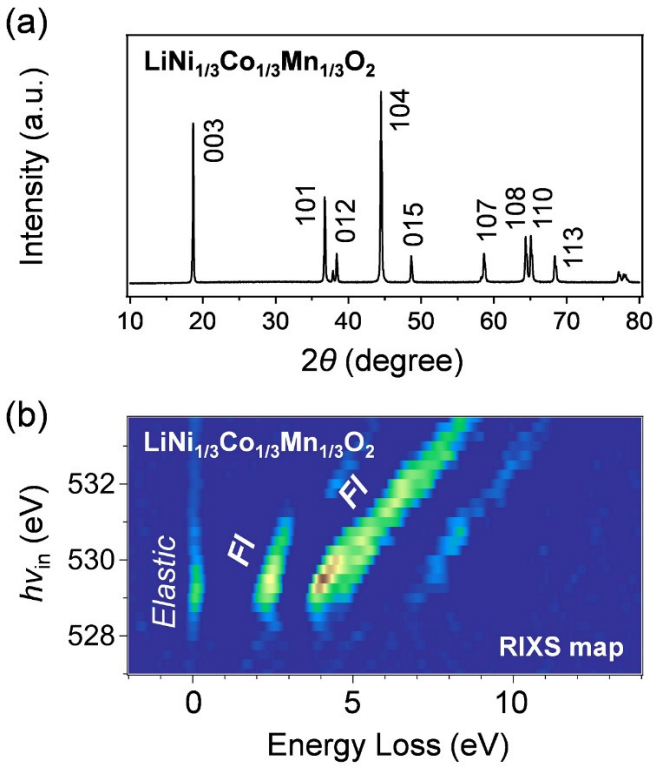


**Figure S4.** (a) X-ray diffraction pattern for $LiNi_{1/3}Co_{1/3}Mn_{1/3}O_2$. (b) Second differential RIXS map for $LiNi_{1/3}Co_{1/3}Mn_{1/3}O_2$. All the peaks are fluorescence-like, indicating that there is no orphaned oxygen 2*p* orbital.

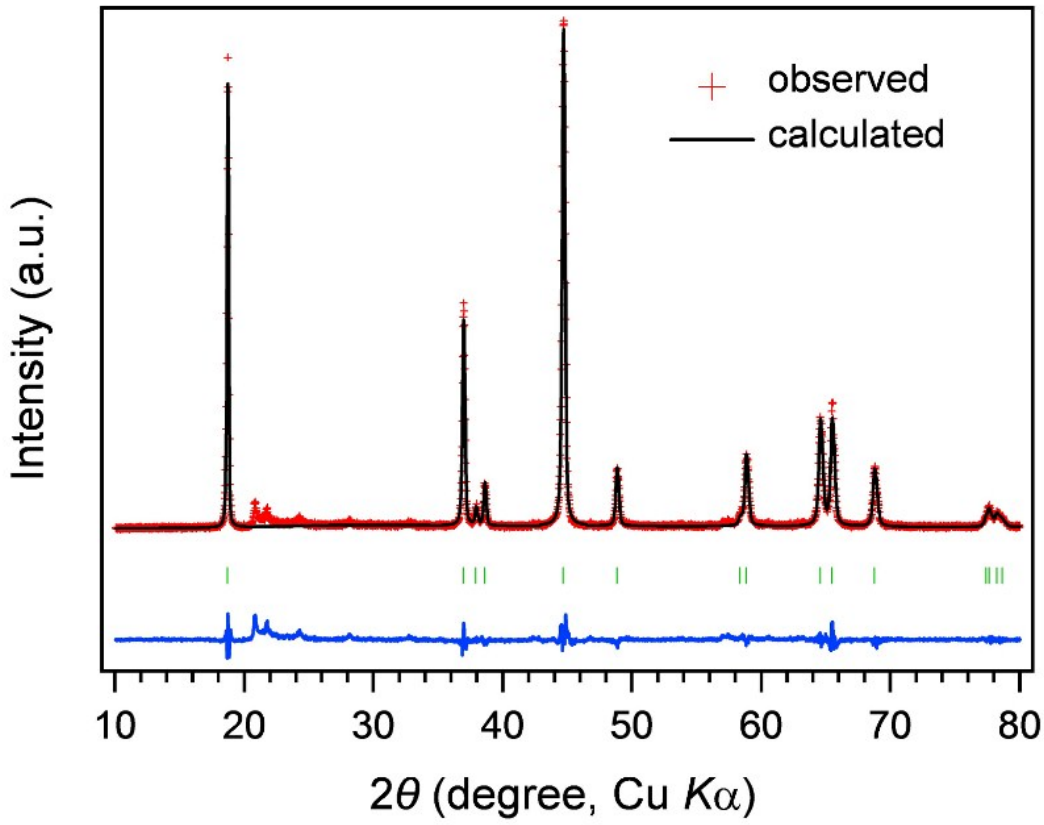


**Figure S5.** X-ray diffraction pattern for $Li_{1.2}Ni_{0.13}Co_{0.13}Mn_{0.54}O_2$. The Rietveld refinement result is also plotted. Superstructure peaks ($20° < 2\theta < 30°$) broadened by stacking faults were ignored in the Rietveld refinement, as the stacking faults are not the focus of this work.

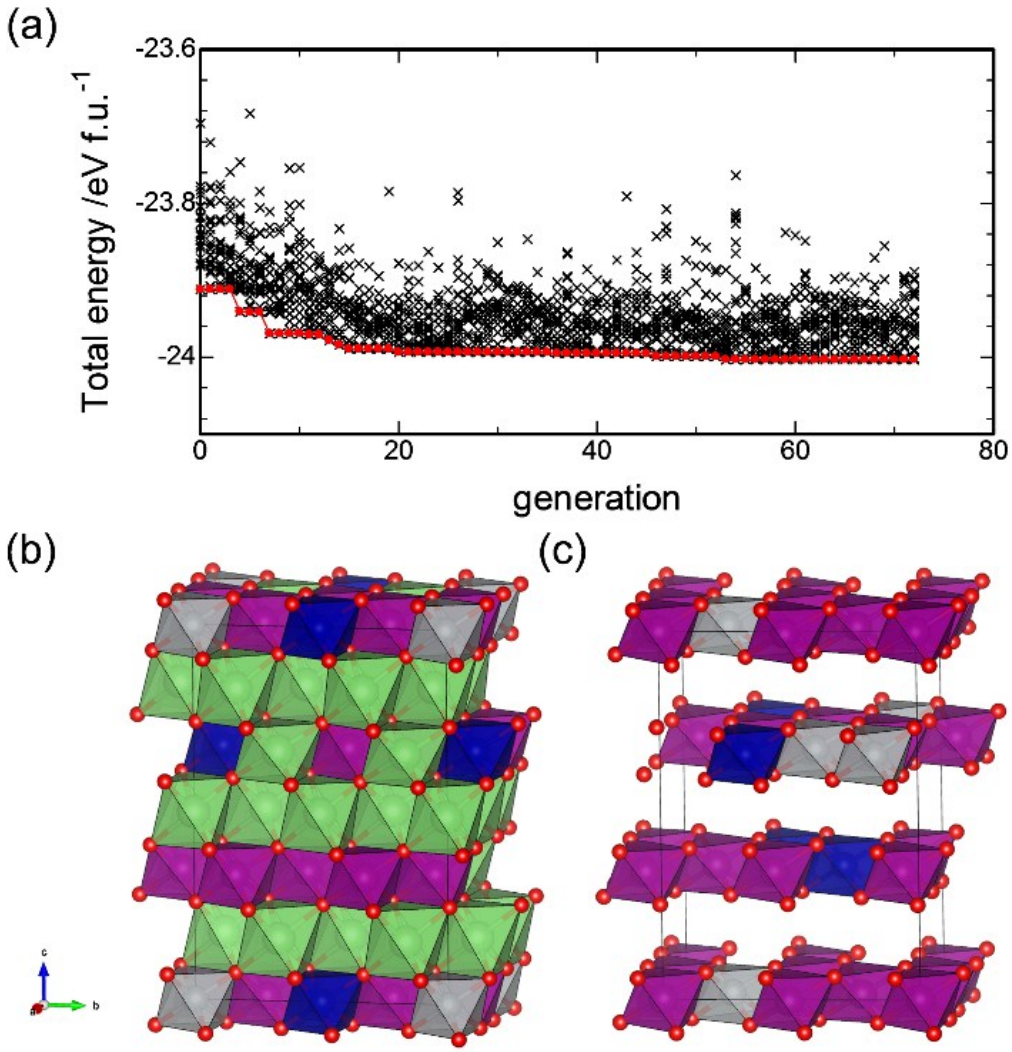


**Figure S6.** (a) Variation of total electron energies for genetic algorithm (GA) driven structures as a function of generation ($Li_{1.20}Ni_{0.13}Co_{0.13}Mn_{0.54}O_2$ as an example). The red symbol indicates the lowest energy of GA generated structures among present and previous generations. Optimized Li/Ni/Co/Mn arrangement for (b) $Li_{1.20}Ni_{0.13}Co_{0.13}Mn_{0.54}O_2$, and (c) $Ni_{0.13}Co_{0.13}Mn_{0.54}O_2$. Green, gray, deep blue, and purple colored octahedra correspond to $LiO_6$, $NiO_6$, $CoO_6$, and $MnO_6$ octahedra, respectively.

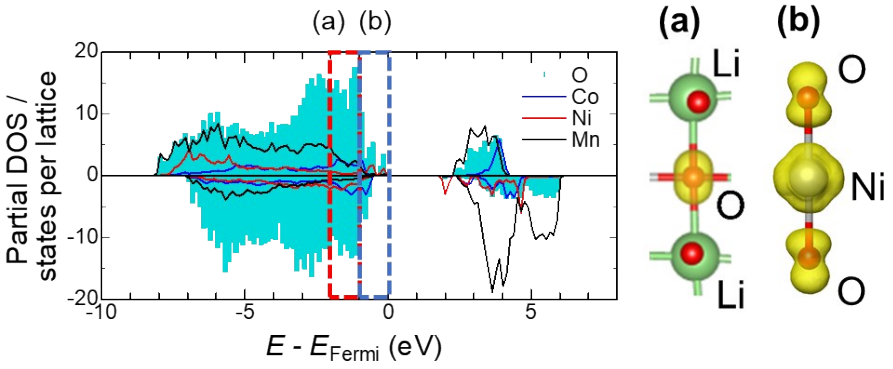


**Figure S7.** The partial density of states (PDOS) for $Li_{1.2}Ni_{0.13}Co_{0.13}Mn_{0.54}O_2$. The spatial electron density along Li−O−Li in the energy region from −2.0 eV to −1.0 eV, and that along O-Ni-O from -1.0 eV to 0 eV versus the Fermi energy is visualized in the panels (a) and (b), respectively.

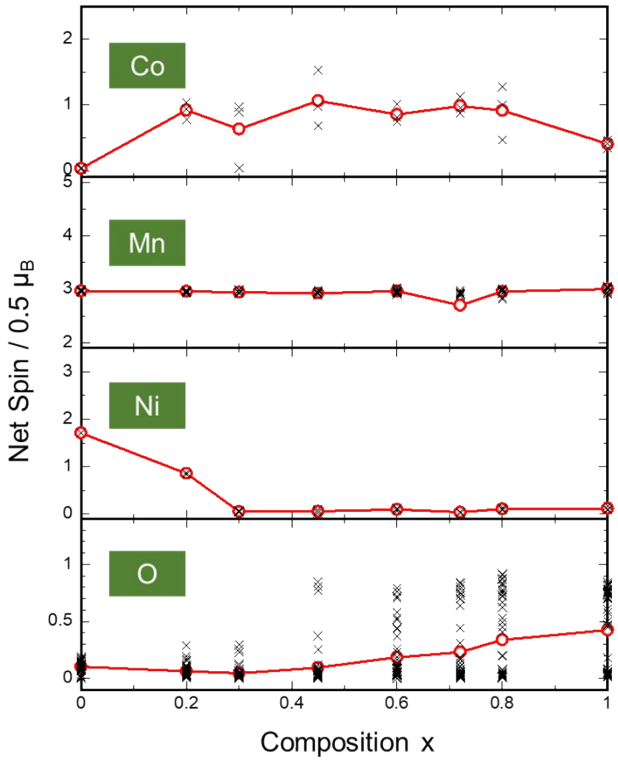


**Figure S8.** The variation of spin integration (SI) values is the total electron-spin difference (net spin) taken as the electron spin up minus the electron spin down as a function of the integration radius of the ion core and composition x in $Li_{1.2-x}Ni_{0.13}Co_{0.13}Mn_{0.54}O_2$. The black and red symbols represent the SI values of individual ions and their average, respectively. The SI values in the figure refer to those at the radius of 1.2 Å. Considering octahedral coordination and low spin configuration for Co and Ni ions, the SI values of $Co^{3+}(t_{2g}^6)$, $Co^{4+}(t_{2g}^5)$, $Mn^{4+}(t_{2g}^3)$, $Ni^{2+}(t_{2g}^6e_g^2)$, $Ni^{3+}(t_{2g}^6e_g^1)$, and $Ni^{4+}(t_{2g}^6)$ correspond to net spin moment of 0, 1, 3, 2, 1, and 0 (unit: 0.5 $\mu_B$), respectively. The SI value of oxide ion, $O^{2-}$ ($2p^6$) is 0, and at oxidized state, such as $O^-$ ($2p^5$), it corresponds to 1.

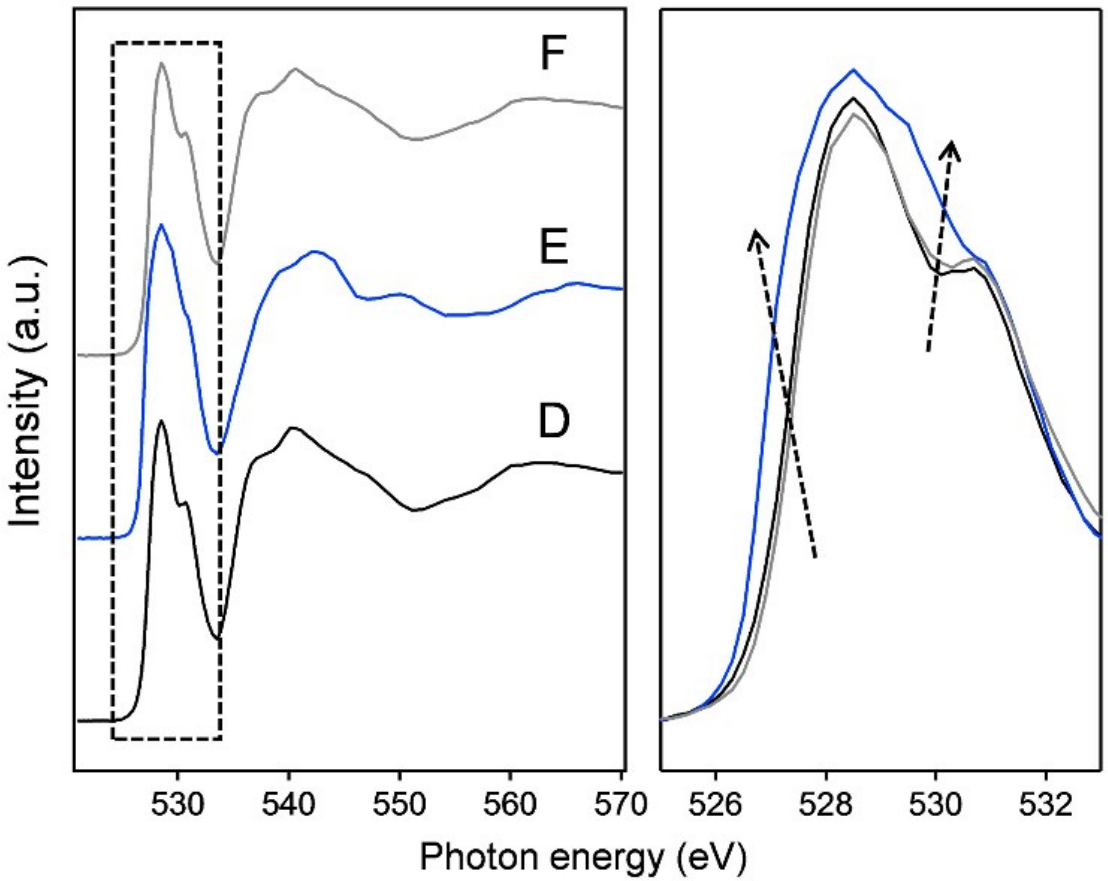


**Figure S9.** Oxygen *K*-edge X-ray absorption spectra in a bulk sensitive fluorescence yield mode for $Li_{1.2-x}Ni_{0.13}Co_{0.13}Mn_{0.54}O_2$ before charge (sample D in Figure 3b), after oxygen oxidation (sample E in Figure 3b), and after discharge (sample F in Figure 3b) during the second cycle.

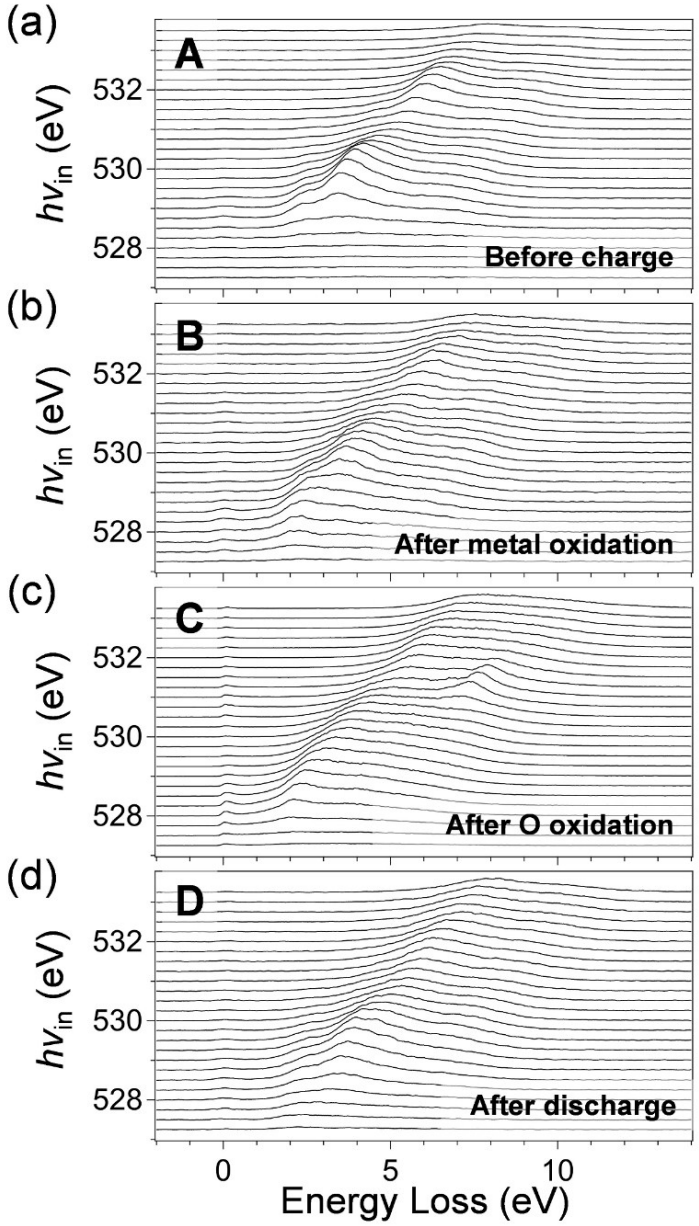


**Figure S10.** Oxygen *K*-edge resonant inelastic X-ray scattering (RIXS) spectra for the samples (a) before charge (sample A in Figure 3b), (b) after metal oxidation (sample B in Figure 3b), (c) after oxygen oxidation (sample C in Figure 3b), and (d) after discharge (sample D in Figure 3b), with the excitation photon energy from 527 to 533.75 eV.

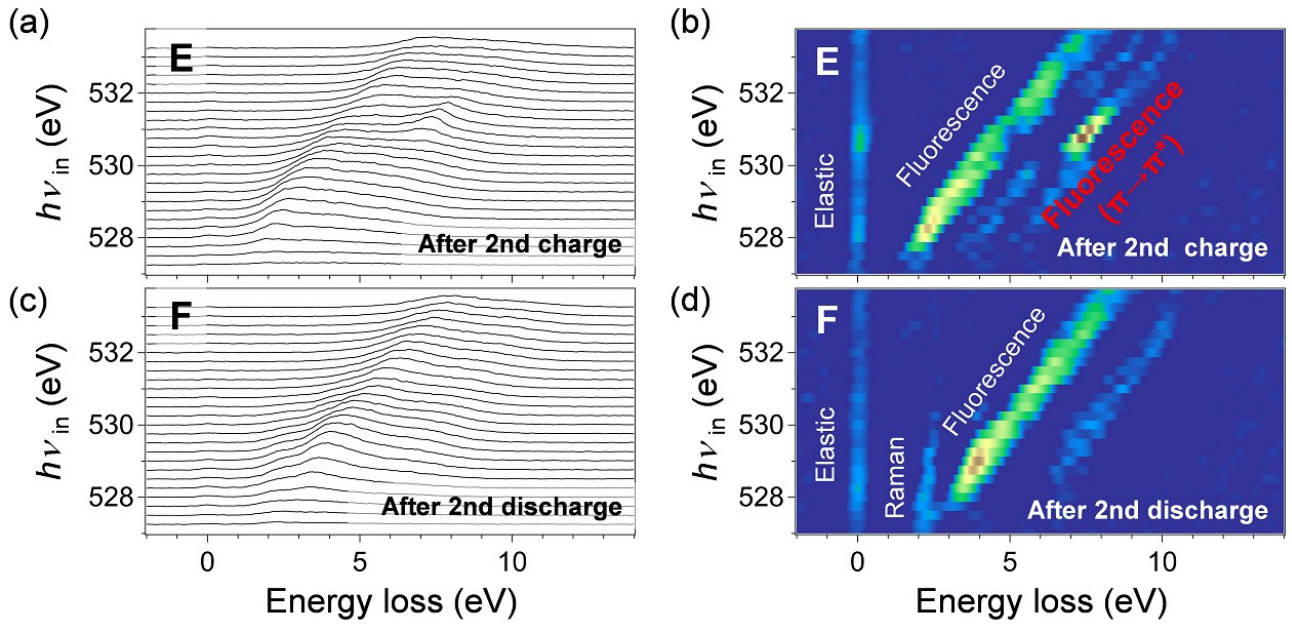


**Figure S11.** Oxygen *K*-edge resonant inelastic X-ray scattering (RIXS) spectra and mappings for the samples (a, b) after charge of 2nd cycle (sample E in Figure 3b), (c, d) after discharge of 2nd cycle (sample F in Figure 3b).

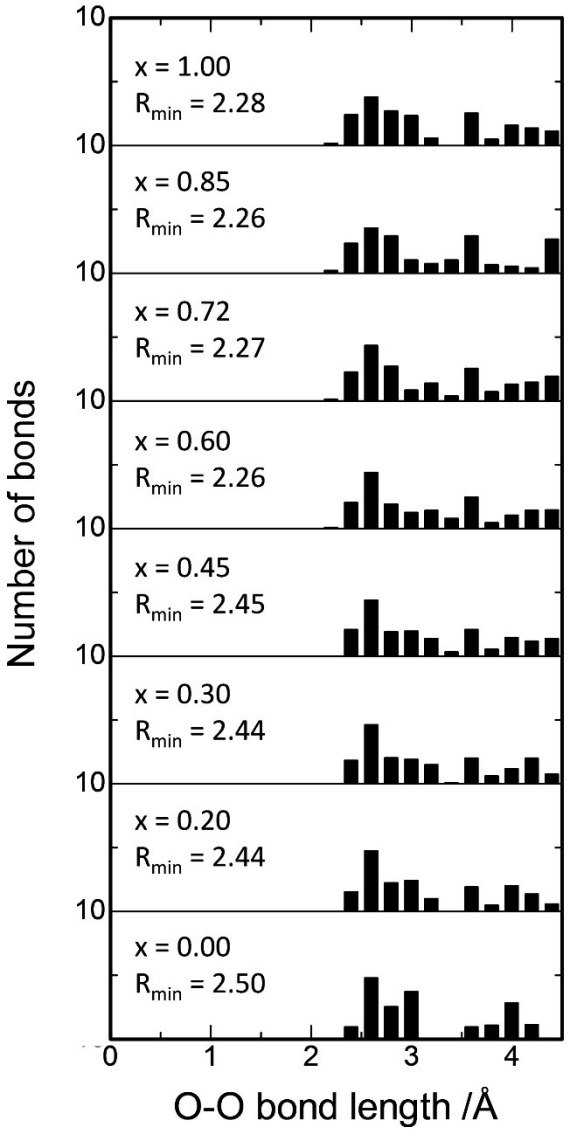


**Figure S12.** DFT calculation results of the distribution of O-O bond distance in $Li_{1.2-x}Ni_{0.13}Co_{0.13}Mn_{0.54}O_2$.

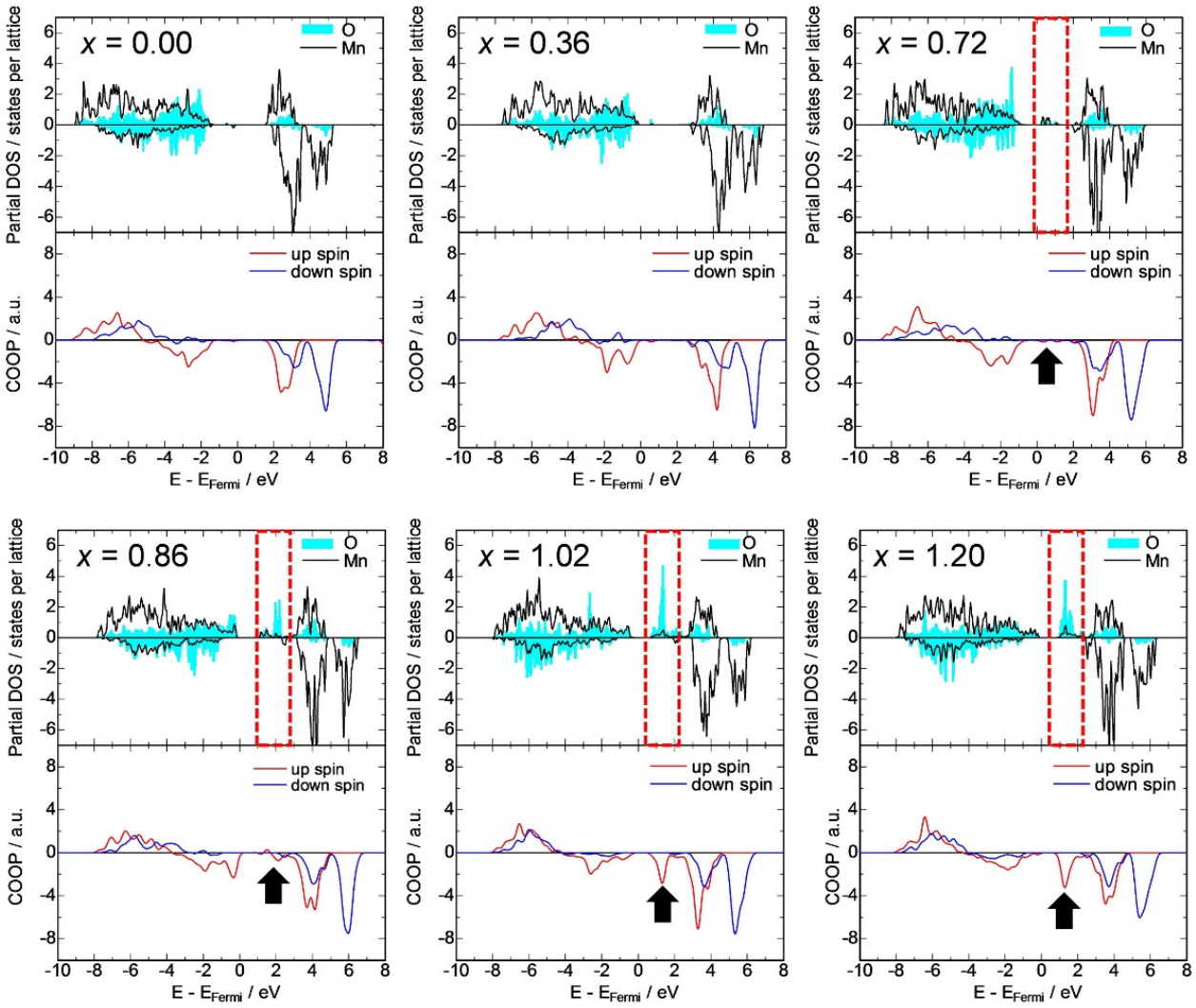


**Figure S13.** Partial density of states (PDOS) and the crystal overlap orbital population (COOP) diagrams selected Mn-O bonds in $Li_{1.2-x}Ni_{0.13}Co_{0.13}Mn_{0.54}O_2$. Red hatched rectangular area in PDOS and black arrows in COOP indicate the enhancement of a bonding character of Mn−O bonds by hole generation on O 2*p* orbitals.

**Table S1.** Structural parameters for $Li_2MnO_3$.

Space group: *Rm*, *a* = 2.8433(2) Å, *c* = 14.218(2) Å

$R_{wp}$ = 15.15%, $R_B$ = 3.45 % (Superstructure peaks excluded)

| Atom | Site | *x* | *y* | *z* | Occupancy | $B_{iso}$ (Å$^2$) |
|---|---|---|---|---|---|---|
| Li | 3*a* | 0 | 0 | 0 | 1 | 1 |
| Li | 3*b* | 0 | 0 | 0.5 | 0.33 | 0.5 |
| Mn | 3*b* | 0 | 0 | 0.5 | 0.67 | 0.5 |
| O | 6*c* | 0 | 0 | 0.2416(7) | 1 | 0.8 |

**Table S2.** Structural parameters for $Li_{1.2}Ni_{0.13}Co_{0.13}Mn_{0.54}O_2$.

Space group: *Rm*, *a* = 2.8491(1) Å, *c* = 14.2237(9) Å

$R_{wp}$ = 11.17 %, $R_B$ = 2.41 % (Superstructure peaks excluded)

| Atom | Site | *x* | *y* | *z* | Occupancy | $B_{iso}$ (Å$^2$) |
|---|---|---|---|---|---|---|
| Li | 3*a* | 0 | 0 | 0 | 1 | 1 |
| Li | 3*b* | 0 | 0 | 0.5 | 0.2 | 0.5 |
| Ni | 3*b* | 0 | 0 | 0.5 | 0.13 | 0.5 |
| Co | 3*b* | 0 | 0 | 0.5 | 0.13 | 0.5 |
| Mn | 3*b* | 0 | 0 | 0.5 | 0.54 | 0.5 |
| O | 6*c* | 0 | 0 | 0.2411(3) | 1 | 0.8 |